nature synthesis

Article

https://doi.org/10.1038/s44160-025-00765-z

Sintering protonic zirconate cells with enhanced electrolysis stability and Faradaic efficiency

Received: 13 April 2024

Accepted: 7 February 2025

Published online: 14 March 2025

Check for updates

Wei Tang[1,2,10], Wenjuan Bian[1,10], Hanping Ding[1,3,10], Yong Ding[4], Zeyu Zhao[1], Quanwen Sun[2], Samuel Koomson[1], You Wang[5], Boshen Xu[6], Pei Dong[6], Dongchang Chen[5], Joshua Y. Gomez[1], Wuxiang Feng[1], Wei Wu[1], Meng Zhou[2], Yanhao Dong[7,8] ✉, Hongmei Luo[2] ✉, Ju Li[8,9] ✉ & Dong Ding[1] ✉

The emerging applications of steam electrolysis and electrochemical synthesis at 300–600 °C set stringent requirements on the stability of protonic ceramic cells, which cannot be met by Ce-rich electrolytes. A promising candidate is Ce-free $BaZr_{0.8}Y_{0.2}O_{3-\delta}$, but its usage has long been hindered due to the high sintering temperatures required for protonic devices. Here we resolved the issue through a co-sintering process, in which the shrinkage stress of a readily sinterable support layer helps to densify the pure $BaZr_{0.8}Y_{0.2}O_{3-\delta}$ electrolyte membrane at low temperatures. This approach eliminates Ce and harmful sintering aids in the dense zirconate electrolyte membrane, thereby enhancing the Faradaic efficiency and electrochemical stability, especially under harsh operating conditions. The protonic zirconate cells have exceptional performance and demonstrate stable high-steam pressure electrolysis up to 0.7 atm steam pressure, −2 A cm^{-2} current density and over 800 h of dynamic operation at 600 °C. Our processing breakthrough enables stabilized protonic cells for demanding applications in future energy infrastructure.

Protonic ceramic fuel cells (PCFCs) are intermediate-temperature electrochemical devices that can efficiently convert the chemical energy of a fuel into electricity below 600 °C (refs. 1–4). There is also growing interest in running these devices in the reverse mode, namely, as protonic ceramic electrolysis cells (PCECs), to produce fuels (for example, H_2) or high-carbon chemicals (for example, ethane to ethylene)[5–7]. As one switches PCFC operation to PCEC, the half-cell reactions taking place at the two electrode/electrolyte interfaces reverse their directions. For example, at the fuel electrode, the hydrogen oxidation reaction $H_2(gas) \rightarrow 2H^+ + 2e^-$ under PCFC operation becomes the hydrogen evolution reaction $2H^+ + 2e^- \rightarrow H_2(gas)$ under PCEC. This would simultaneously reverse the sign of the electrode overpotentials, which sets more extreme and demanding electrochemical conditions in PCECs, especially under high current densities that are desirable for higher production rates[8–10]. Therefore, stability is a key issue to be addressed for practical PCECs applications.

The state-of-the-art architecture of PCFCs/PCECs is a sandwich structure with a porous fuel electrode support layer (a ~600-μm-thick

[1]Energy and Environment Science and Technology, Idaho National Laboratory, Idaho Falls, ID, USA. [2]Department of Chemical and Materials Engineering, New Mexico State University, Las Cruces, NM, USA. [3]School of Aerospace and Mechanical Engineering, University of Oklahoma, Norman, OK, USA. [4]School of Materials Science and Engineering, Georgia Institute of Technology, Atlanta, GA, USA. [5]Department of Chemistry and Chemical Biology, University of New Mexico, Albuquerque, NM, USA. [6]Department of Mechanical Engineering, George Mason University, Fairfax, VA, USA. [7]State Key Lab of New Ceramics and Fine Processing, School of Materials Science and Engineering, Tsinghua University, Beijing, China. [8]Department of Nuclear Science and Engineering, Massachusetts Institute of Technology, Cambridge, MA, USA. [9]Department of Materials Science and Engineering, Massachusetts Institute of Technology, Cambridge, MA, USA. [10]These authors contributed equally: Wei Tang, Wenjuan Bian, Hanping Ding. ✉e-mail: dongyanhao@tsinghua.edu.cn; hluo@nmsu.edu; liju@mit.edu; dong.ding@inl.gov

composite made of the electrolyte materials and NiO, which is reduced to metallic Ni before the operation that also generates porosity), a ~20-μm-thick dense electrolyte membrane in the middle and a thin, porous oxygen electrode (typically a perovskite structure with mixed ionic and electronic conductivities). The preferred protonic electrolyte is perovskite ABO_3. The most popular options include $BaCeO_3$ co-doped with Zr, Y and Yb, such as $BaCe_{0.7}Zr_{0.1}Y_{0.1}Yb_{0.1}O_{3-\delta}$ (BCZYYb)[11]. Although still requiring a relatively high sintering temperature of ~1,450 °C to densify, BCZYYb provides high proton conductivity at 300–600 °C and sufficient stability for PCFC operations. However, BCZYYb and other Ce-rich perovskite electrolytes in general show poor chemical compatibility with acidic atmospheres (for example, containing H_2O and CO_2) on the oxygen electrode side and poor electrochemical stability against reduction on the fuel electrode side[1,12–15]. The situation becomes even worse in high-current density and/or high-steam pressure PCEC operations. Here, a high steam pressure (acidic) is preferred because (1) it lowers the open-circuit voltage (OCV; for example, increasing the H_2O partial pressure from 10% steam–90% air to 70% steam–30% air lowers the OCV by 0.094 V at 600 °C) that the applied voltage must overcome to drive the electrolysis reaction and (2) it suppresses hole leakage (which is especially problematic under high current densities), thus increasing the Faradaic/energy efficiency.

The solution to the high-steam pressure corrosion problem is supposed to be straightforward: along with the development of $BaCeO_3$-based electrolytes, $AZrO_3$-based ones (A = Ba, Sr, Ca and so on) have also been explored, with a long history dating back to the 1980s[16–18]. The latter show adequate proton conductivity in the dense form but are too refractory to be sintered[19]. For example, $BaZr_{0.8}Y_{0.2}O_{3-\delta}$ (BZY) typically requires ≥1,600 °C sintering temperature for both pellets and membranes in the co-sintered fuel electrode/electrolyte bilayer[20–22]. This sinterability conundrum for dense electrolyte membrane not only increases the energy and cost for processing, but also causes detrimental effects to the electrochemical cells, such as Ba loss (due to volatilization) and severe side reactions between NiO and the electrolyte. As a result, $BaZrO_3$-based electrochemical cells do not show as high performance as what has been demonstrated by BCZYYb cells. However, aside from the processing conundrum for dense electrolyte membrane, BZY does show much better chemical stability against acidic atmospheres[20,21]. And even in Ce-rich perovskites, increasing the Zr cation percentage to 40% at the B site can largely improve the CO_2 stability as recently demonstrated by $BaCe_{0.4}Zr_{0.4}Y_{0.1}Yb_{0.1}O_{3-\delta}$ (ref. 23).

In view of the stability bottleneck in developing practical PCECs, we dedicated our work to advancing the processing science of Ce/sintering aid-free BZY electrolytes and evaluated the intrinsic performance of BZY full cells, especially for high-steam pressure electrolysis. We successfully decreased the pressureless sintering temperature of BZY (without any sintering aids that may lead to proton traps or resistive grain boundary phases) to a low one of 1,450 °C. This enables high proton conductivity and high electrochemical performance for BZY full cells that far exceed literature reports in relevant systems. Our results illustrate the promise of protonic zirconate electrolytes for use in high-performance electrolysers with stringent stability requirements. More broadly speaking, as the operations of many electrochemical energy devices are being pushed towards extreme conditions to maximize efficiency and energy density, we call attention to the activity–stability trade-off and focus on durable materials/devices.

Solution to the BZY conundrum

PCFC/PCEC full cells are typically sintered in two steps in air. First, the fuel electrode/electrolyte bilayer (the half-cell) is sintered at a higher temperature T_1 (~1,450 °C) to obtain a dense electrolyte. In the same T_1 step, the fuel electrode, consisting of NiO blended with some electrolyte material, is also sintered to full density, and its porosity will be 'regenerated' to allow for gas permeation when NiO is reduced to metallic Ni (~40% volume shrinkage) before electrochemical operation of the full cell. In the second step, the oxygen electrode is attached to the electrolyte surface of the sintered half-cell at a lower temperature T_2 (~1,000 °C). Once sufficient diffusional bonding to the electrolyte is ensured, a lower T_2 is preferred to minimize coarsening of the porous oxygen electrode materials for optimal catalytic activity. Conventionally, when preparing the full cell, the same fast ion conductor is used in the electrolyte and the composite fuel electrode (as well as in the composite oxygen electrode until the development of single-phase oxygen electrode using mixed ionic and electronic conductors) to minimize sintering stress, thermal expansion mismatch and materials incompatibility. This practise has been routinely adopted since the early development of solid oxide fuel cells (SOFCs)/solid oxide electrolysis cells (SOECs), followed by their intermediate-temperature successor, PCFCs/PCECs.

However, in contrast to the high sinterability of yttria-stabilized zirconia and gadolinium-doped ceria electrolytes used in O^{2-}-based SOFCs/SOECs, perovskite-structure protonic electrolytes are known to be difficult to sinter because of sluggish B site cation diffusion. For example, despite a similar melting point for zirconia (2,715 °C) and barium zirconate (2,700 °C), BZY pellets/membranes require ≥1,600 °C to sinter compared with ~1,300 °C for yttria-stabilized zirconia membranes; similarly, for ceria (2,400 °C) and barium cerate (>2,150 °C), BZCYYb membranes require >1,400 °C to sinter, while gadolinium-doped ceria membranes require only ~1,250 °C (refs. 24–31) (here, also note that ceria/cerates are easier to sinter than zirconia/zirconates because of lower melting points and the partial reduction of Ce^{4+} to Ce^{3+} at high temperatures that facilitates high-valence cation diffusion[32]). The sinterability issue of perovskite protonic electrolytes results in processing difficulties in T_1 sintering of the half-cell, and a weak oxygen electrode/electrolyte interface in T_2 sintering of the full cell. Pure BZY is particularly challenging to sinter in half-cell geometry at a technologically accessible temperature range (for example, ≤1,450 °C) so that its applications in PCFCs/PCECs remain largely unexplored. A tentative solution to this BZY membrane conundrum is to use low-melting-point sintering aids such as NiO, ZnO and CuO (effectively lowering T_1 to ~1,450 °C), but they would cause detrimental effects to the proton conductivity and stability under extreme conditions, which deteriorates BZY's benefits over BCZYYb[33–37].

We now resolve the BZY conundrum by the following full cell structure redesign (Fig. 1a). We blended Ce-rich, high-sinterability BCZY with NiO (BCZY + NiO) which is utilized as the support layer. A buffer layer consisting of blended BZY and NiO, sandwiched between the support layer and the BZY electrolyte, was used to minimize sintering/thermal stresses and to block Ce diffusion from BCZY to the dense BZY electrolyte membrane. During sintering, two pieces of identical BCZY + NiO|BZY + NiO|BZY trilayers were placed face to face to minimize the Ba loss. In our design, the faster densification of the thicker BCZY + NiO support layer would transmit compressive stress to both the laminated BZY + NiO buffer layer and the BZY electrolyte. This design helps the co-sintering of the multilayer structure, provided that sintering and thermal stresses are manageable to prevent delamination in the full cell processing. Our design is based on two rationales. First, for PCFCs/PCECs, the fuel electrode/electrolyte interface is substantially stronger than the oxygen electrode/electrolyte interface, making the latter unlikely to be the bottleneck for the mechanical stability of the full cell. Second, the perovskite structure accommodates a wide variety of cations, and $BaZrO_3$ and $BaCeO_3$ are expected to form a complete solid solution across the entire composition range with only minor changes in lattice parameters, polyhedral distortions and local symmetry. Therefore, the material incompatibility between the dense BZY electrolyte membrane and BCZY + NiO support should be minimal.

We started by establishing some baseline for the BZY sintering conundrum. We confirmed that a sintering aid-free BZY pellet cannot be fully densified even at 1,600 °C for 10 h (microstructure shown in Supplementary Fig. 1) and reaches only 72% relative density at 1,500 °C

https://doi.org/10.1038/s44160-025-00765-z

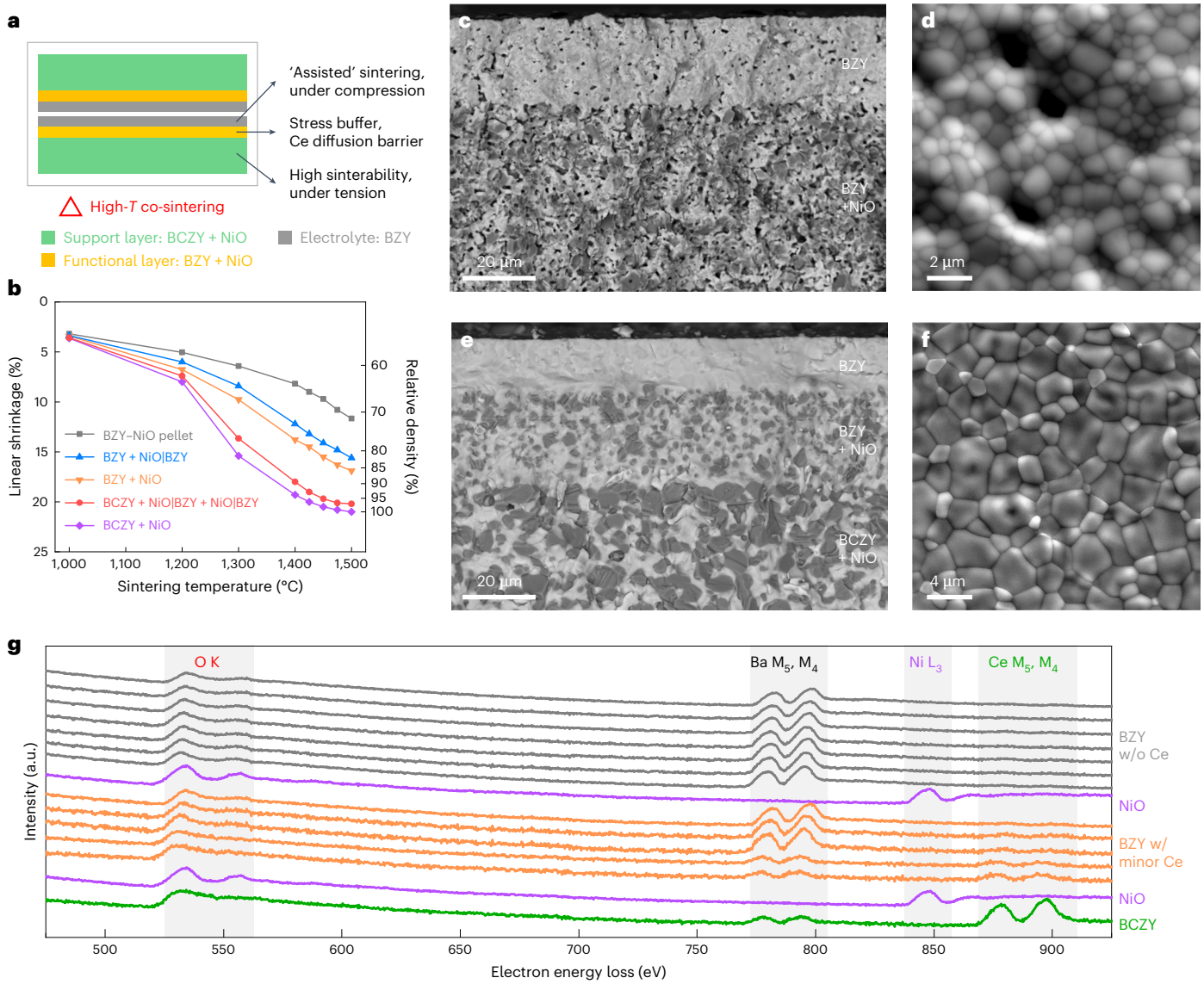

Fig. 1 | Redesigned half-cell to resolve the BZY membrane sintering conundrum. a, A schematic of the half-cell design and face-to-face sintering geometry. **b**, Linear shrinkage and estimated relative density of different samples (BZY–NiO pellet, laminated BZY + NiO|BZY bilayer tape, BZY + NiO tape, laminated BCZY + NiO|BZY + NiO|BZY trilayer tape and BCZY + NiO tape) at different sintering temperatures for 10 h in air. **c**,**d**, The microstructure of the fracture surface (**c**) and electrolyte surface (**d**) of BZY + NiO|BZY sintering at 1,450 °C for 10 h in air. **e**,**f**, The microstructure of the fracture surface (**e**) and electrolyte surface (**f**) of BCZY + NiO|BZY + NiO|BZY sintering at 1,450 °C for 10 h in air. **g**, EELS spectra of BCZY + NiO|BZY + NiO|BZY sintering at 1,450 °C for 10 h in air (BCZY + NiO layer with strong Ce peak, BZY + NiO layer with minor (w/minor) Ce, and BZY layer without (w/o) Ce). The grey shading shows the electron loss range of interest. Details for the collection spots are shown in Supplementary Fig. 6.

for 10 h. For tape casting-derived samples, we measured the linear shrinkage $\Delta L/L_0 = (L_0 - L)/L_0$ (where L_0 and L denote the dimension before and after sintering, respectively) along the diameter direction, which can be used to estimate the sintered density, and compared it with that of the BZY pellet. We found that BZY + NiO tape can be better densified (Fig. 1b) because NiO is less refractory and also helps densify BZY as a sintering aid. Benefiting from this, the BZY + NiO|BZY bilayer also shows improved densification over the BZY pellet, yet it still cannot reach full density below 1,500 °C. When sintered at 1,450 °C (preferred T_1 for PCFC/PCEC processing) for 10 h, the BZY electrolyte contains many pores as shown by the fracture surface (Fig. 1c) and the electrolyte surface (Fig. 1d) under a scanning electron microscope (SEM), and the estimated relative density is between 78% and 85% (explained later). The residual porosity would lower the proton conductivity and cause gas leakage in electrochemical cells. Meanwhile, without entering final stage sintering (>~92% relative density when pore channels break into isolated pores), the strong pore pinning effect suppresses grain growth[38], thus producing a fine grain size (1.1 μm at the electrolyte surface; Fig. 1d) that further lowers the proton conductivity due to the ion-blocking grain boundaries[39].

The high sinterability of BCZY is demonstrated by the BCZY + NiO tape (Fig. 1b) that can be fully densified at ≤1,500 °C as shown by the SEM in Supplementary Fig. 2. The densification rate of the BCZY + NiO tape indicated by linear shrinkage is much faster than the BZY pellet, BZY + NiO and BZY + NiO|BZY. This benefit translates to our newly designed BCZY + NiO|BZY + NiO|BZY trilayer, which shows high density (fracture surface in Fig. 1e and the electrolyte surface in Fig. 1f) when sintered at 1,450 °C for 10 h (when sintered at 1,350 °C for 10 h, the BZY layer in the BCZY + NiO|BZY + NiO|BZY trilayer has a relatively porous structure, as shown in Supplementary Fig. 3; when sintered at 1,400 °C for 10 h, it has a dense structure and fine grain size, as shown in Supplementary Fig. 4.) Remarkably, good interfacial bonding is demonstrated,

https://doi.org/10.1038/s44160-025-00765-z

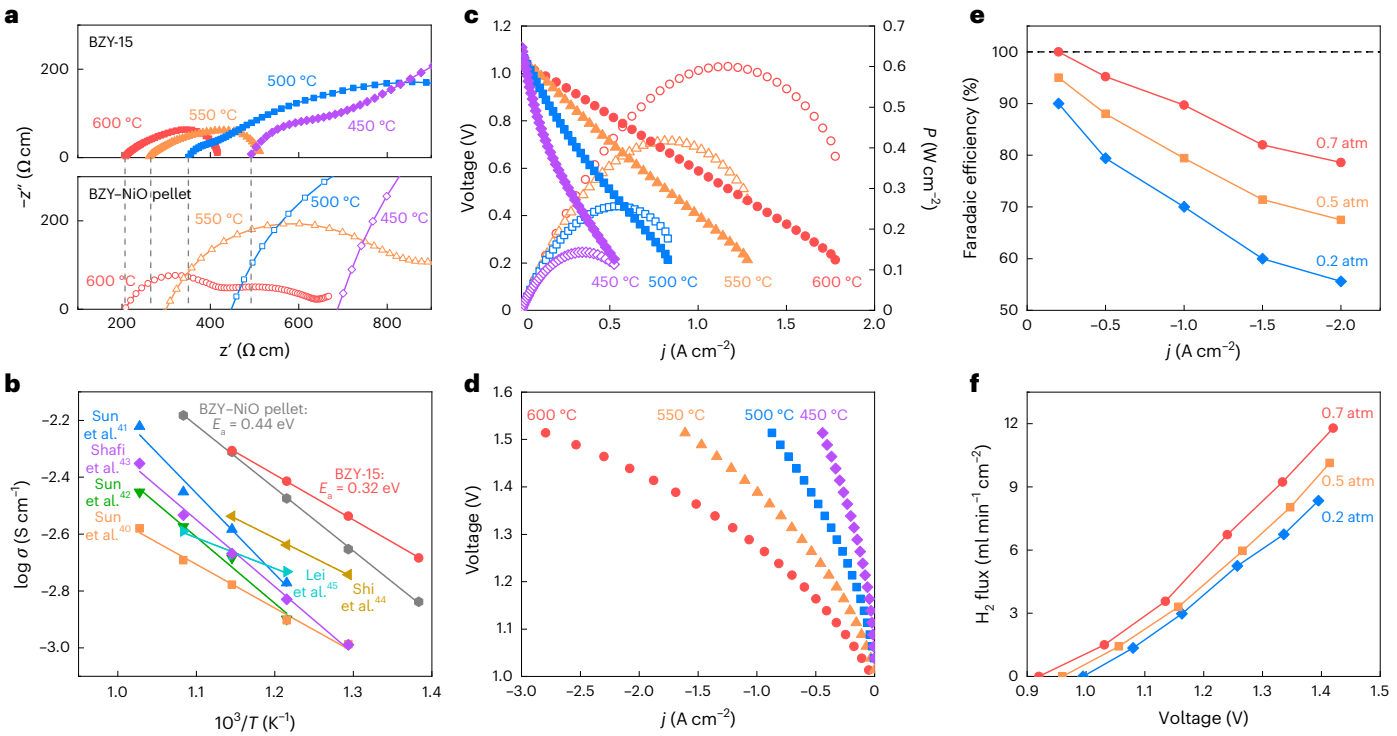

Fig. 2 | Electrochemical performance of BZY-15 full cells. a, Spectra of the reduced complex impedance. z' and z'' denote the real and imaginary part of the reduced complex impedance, respectively. The dashed lines show the intercept with the x axis. **b**, A comparison of obtained proton conductivity, σ, with the literature[40–45]. **c**,**d**, PCFC performance (**c**) and PCEC performance (**d**) of the BZY-15 cell at different current densities, j, at 450–600 °C. **e**, A comparison of the Faradaic efficiency of the BZY-15 cell under PCEC operation and different steam pressures (balanced with air, for example, 0.2 atm steam denotes 20% H_2O + 80% air). **f**, A comparison of the H_2 flux of the BZY-15 cell under PCEC operation and different steam pressures. Temperature: 600 °C; feedstock for fuel electrode: pure H_2.

and neither shape distortion nor delamination is observed (see photos of sintered full cells in Supplementary Fig. 5). For better quantifications, we shall assume a similar relative density for all the tapes, isotropic sintering behaviour and a baseline of 100% relative density for BCZY + NiO sintered at 1,500 °C for 10 h (with 21% linear shrinkage). This allows us to estimate the relative density by $0.79^3/(L/L_0)^3$ as shown by the y axis in Fig. 1b, right. Thus, the estimated relative density is 95% for the BCZY + NiO-supported trilayer BCZY + NiO|BZY + NiO|BZY versus 78% for the BZY + NiO-supported bilayer BZY + NiO|BZY when sintered at 1,450 °C for 10 h. For multilayer co-sintering, the thickness direction is not constrained, so its sintering should be easier than the two in-plane directions. This sets another boundary for the estimated relative density by $0.79^2/(L/L_0)^2$. Thus, the estimated relative density is 97% for BCZY + NiO|BZY + NiO|BZY versus 85% for BZY + NiO|BZY when sintered at 1,450 °C for 10 h. Both estimations show much higher densities for our new half-cell design, which is higher than the >95% threshold that is typically required for SOFC/SOEC/PCFC/PCEC electrolytes. In addition, benefitting from accelerated grain growth in the final stage sintering, a larger grain size of the electrolyte is also obtained (3.1 µm at the electrolyte surface; Fig. 1f), which is also desirable from an ionic-conductivity perspective.

To prove the well-sintered BZY is assisted by BCZY + NiO rather than Ce doping, we conducted electron energy loss spectroscopy (EELS) measurements (Fig. 1g) under a scanning transmission electron microscope (STEM) over a large area (Supplementary Fig. 6). Compared with the strong Ce M_4 and M_5 edge peaks in BCZY (Fig. 1g, green curve, and Supplementary Fig. 6, coarse grain structure), the peaks are much weaker in the BZY grains of the BZY + NiO layer (with gradually decreasing signals from the BCZY + NiO side to the BZY electrolyte side; Fig. 1g, orange curves, and Supplementary Fig. 6, fine grain structure) and no Ce peaks can be observed in the BZY electrolyte layer (Fig. 1g, grey curves, and Supplementary Fig. 6, fine grain structure) (the two purple curves in Fig. 1g show EELS spectra with an Ni L_3-edge peak for NiO grains in the composite layers). This supports the design of BZY + NiO buffer layer as a Ce diffusion barrier and the interdiffusion between BCZY + NiO and BZY + NiO results in a Ce concentration gradient and graded microstructure, which blunts the sintering/thermal stress concentration at a sharp interface and improves interfacial bonding. Therefore, our gradient design offers a sintering aid-free and complete solution to the dense BZY membrane conundrum.

High-performance BZY cells

To evaluate the electrochemical properties, we first performed electrochemical impedance spectroscopy (EIS) at 450–600 °C and compared the proton conductivity of the BZY electrolyte in sintered full cells (with an electrolyte thickness of ~15 µm, the cells are thus denoted as BZY-15 hereafter) with the one in the dense BZY pellet with a 1 wt% NiO sintering aid (abbreviated as BZY–NiO pellet, sintered at 1,600 °C for 10 h in air; microstructure and pellet size shown in Supplementary Fig. 7, pellet thickness of 680 µm). The grain size distributions of BZY-15 and BZY–NiO are compared in Supplementary Fig. 8. For fair comparison, the real (Z') and imaginary (Z'') parts of the EIS were normalized by the electrolyte's geometry to obtain the thickness (L) independent real ($z' = Z'/L$) and imaginary ($z'' = Z''/L$) parts (Fig. 2a). At such temperatures, the depressed semicircles come from interfacial kinetics at the electrodes, and the left intercept with the x axis can be interpreted as ohmic resistivity mainly from proton transport inside the electrolyte. Clearly, BZY-15 shows comparable ohmic resistivity to the BZY–NiO pellet at 600 °C and lower ohmic resistivity at lower temperatures. The comparison is further made in the Arrhenius plot (Fig. 2b), where the proton conductivity σ of the dense BZY electrolyte membrane in BZY-15 shows weaker temperature dependence and thus

https://doi.org/10.1038/s44160-025-00765-z

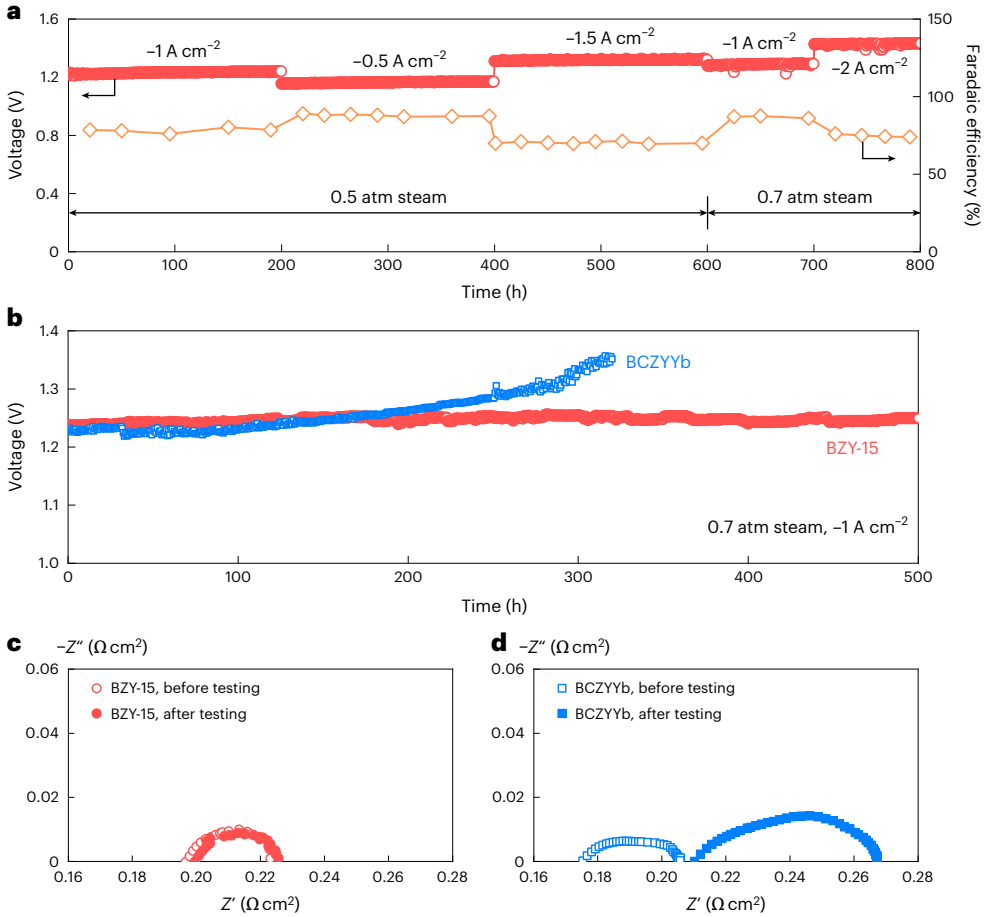

Fig. 3 | Stability under high-steam pressure electrolysis. a, Cell voltage and Faradaic efficiency during long-term PCEC operations of BZY-15 cell at 600 °C. Feedstock for fuel electrode: pure H_2. Other testing conditions are specified in the main text. **b**, Cell voltage during long-term PCEC operations of BZY-15 and BCZYYb cells at −1 A cm^{-2} and 0.7 atm steam at 600 °C. Feedstock for fuel electrode: pure H_2. **c**, EIS measured at a d.c. bias of −1 A cm^{-2} before and after 500 h of testing of the BZY-15 cell in **b**. **d**, EIS measured at a d.c. bias of −1 A cm^{-2} before and after 320 h of testing of the BCZYYb cell in **b**.

smaller activation energy E_a (0.32 eV) than that of the BZY–NiO pellet (E_a = 0.44 eV, which indicates the detrimental effect of the NiO sintering aid to proton conductivity). The proton conductivity achieved in BZY-15 is much higher than those reported for Ce-free $BaZrO_3$-based full cells in the literature (all of which used sintering aids, except for Lei et al.)[40–45].

Under PCFC operations (Fig. 2c, 97% H_2 + 3% steam for the hydrogen electrode and air for the oxygen electrode), the BZY-15 cell shows high performance with a peak power density P_{max} of 0.60 W cm^{-2} at 600 °C, 0.42 W cm^{-2} at 550 °C, 0.26 W cm^{-2} at 500 °C and 0.14 W cm^{-2} at 450 °C. Under PCEC operations (Fig. 2d, H_2 for the hydrogen electrode and air + 20% steam for the oxygen electrode), the BZY-15 cell shows high current densities of −1.14 A cm^{-2} at 600 °C, −0.67 A cm^{-2} at 550 °C, −0.34 A cm^{-2} at 500 °C and −0.17 A cm^{-2} at 450 °C, at an applied voltage of 1.3 V. Considering the encouraging results, we shall first turn to the challenging electrolysis leakage and stability issues before engineering the components for optimized electrochemical performance.

Stable high-steam pressure electrolysis

A more stringent yet rewarding application of BZY full cells is to conduct high-steam pressure electrolysis, which is known to cause corrosion problems in Ce-rich protonic ceramic cells due to the incompatibility of $BaCeO_3$ with acidic H_2O vapour. Enabling high-steam pressure electrolysis not only decreases the OCV (the voltage barrier to overcome to drive H_2O splitting instead of H_2 oxidation), but also increases the Faradaic efficiency by suppressing the hole leakage through the electrolyte (a known problem for PCECs). The latter can be understood from the following defect reactions using the Kröger–Vink notation

$$H_2O\,(g) + V_O^{\bullet\bullet} + O_O^{\times} \overset{K_1}{\Rightarrow} 2OH_O^{\bullet}, \quad (1)$$

$$O_2\,(g) + 2V_O^{\bullet\bullet} \overset{K_2}{\Rightarrow} 2O_O^{\times} + 4h^{\bullet}, \quad (2)$$

where K_1 and K_2 are the reaction constant for defect reactions (1) and (2), respectively. In the Kröger–Vink notation, V denotes vacancies. Using the law of mass action, one obtains

$$\frac{[OH_O^{\bullet}]}{[h^{\bullet}]} = K_1^{1/2} K_2^{-1/4} P_{H_2O(g)}^{1/2} P_{O_2(g)}^{-1/4} [O_O^{\times}] \quad (3)$$

where $[i]$ denotes the concentration of species i, $P_{H_2O(g)}$ denotes the partial pressure of water vapour and $P_{O_2(g)}$ denotes the partial pressure of oxygen gas. Assuming constant mobilities for protons and hole polarons[46], it is clear that increasing H_2O partial pressure on the oxygen electrode decreases electronic (hole) leakage current and improves the Faradaic efficiency (the ratio of protonic current density to the total current density). Meanwhile, for higher-current density PCEC operations, lowered Faradaic efficiency is expected due to a larger anodic overpotential that sets a more oxidizing condition (higher equilibrium oxygen partial pressure) at the oxygen electrode/electrolyte interface. For hole-dominated electronic leakage (p-type electronic

https://doi.org/10.1038/s44160-025-00765-z

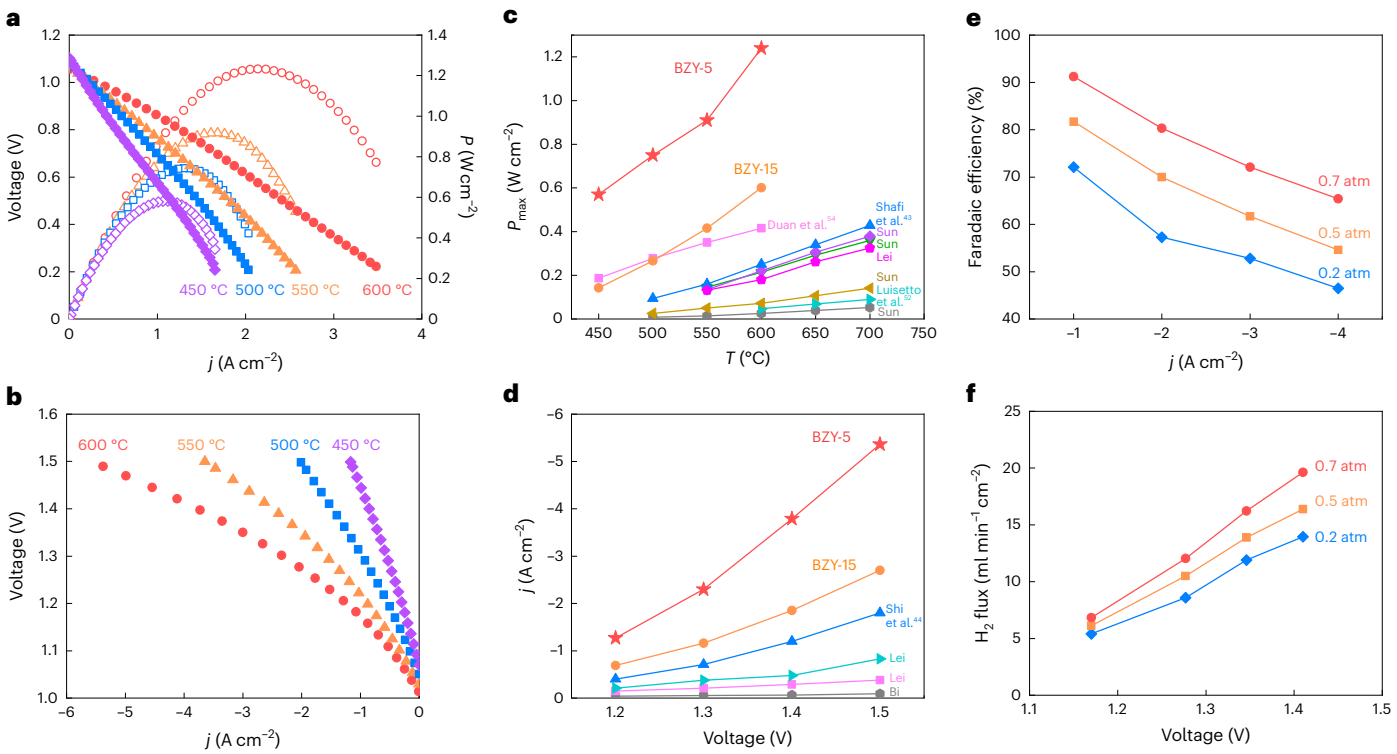

Fig. 4 | Electrochemical performance of BZY-5 full cells with ultrathin electrolyte. **a**,**b**, The PCFC (**a**) and PCEC (**b**) performance of the BZY-5 cell at different current densities, *j*, at 450–600 °C. **c**,**d**, A comparison of PCFC (**c**) and PCEC (**d**) performance with the literature[40–45,51–56]. **e**, A comparison of the Faradaic efficiency of the BZY-5 cell under PCEC operation and different steam pressures (balanced with air, for example, 0.2 atm steam denotes 20% H_2O + 80% air). **f**, A comparison of the H_2 flux of the BZY-5 cell under PCEC operation and different steam pressures. Temperature, 600 °C; feedstock for fuel electrode, pure H_2.

conductivity), the extreme boundary condition is further translated into the bulk electrolyte by a sharp transition in the oxygen chemical potential, which would expose a majority part of the electrolyte membrane to very high oxygen partial pressure[10,47].

The Faradaic efficiency of BZY-15 cells was measured under different steam pressures (balanced by air) and current densities at 600 °C (Fig. 2e). We found increasing steam pressure from 0.2 atm to 0.7 atm brings 90% Faradaic efficiency to 100% at −0.2 A cm^{-2}. The improvement applies to larger electrolysis current densities up to −2 A cm^{-2}, where 79% Faradaic efficiency is demonstrated under 0.7 atm steam pressure versus 56% under 0.2 atm. The improved Faradaic efficiency and lowered OCV by high-steam pressure allow us to generate larger H_2 outflux under the same applied voltage (Fig. 2f), with 6.73 ml min^{-1} cm^{-2} under 1.24 V and 11.79 ml min^{-1} cm^{-2} under 1.42 V.

We next evaluated the long-term stability of BZY-15 cell for high-steam pressure electrolysis at 600 °C. We set up a harsh, continuous PCEC testing schedule with a total time of 800 h as follows: (1) at −1 A cm^{-2} and 0.5 atm steam for 200 h, (2) at −0.5 A cm^{-2} and 0.5 atm steam for 200 h, (3) at −1.5 A cm^{-2} and 0.5 atm steam for 200 h, (4) at −1 A cm^{-2} and 0.7 atm steam for 100 h and (5) at −2 A cm^{-2} and 0.7 atm steam for 100 h. As shown in Fig. 3a, under a constant applied current density for each testing step, there is minimal increase in the voltage, and the Faradaic efficiency (measured intermittently) remains stable, demonstrating excellent stability in the electrochemical performance. After the 800 h test, we fractured the BZY-15 cell and characterized the microstructure of the cross-section (the fracture surface) under SEM (Supplementary Fig. 9). We found that the oxygen electrode remained intact with the electrolyte and no electrolyte membrane cracking was observed.

To directly compare the stability of BZY and BCZYYb full cells, we tested both cells under PCEC operations at −1 A cm^{-2} and 0.7 atm steam at 600 °C. As shown in Fig. 3b, under a constant current density, the BCZYYb cell has a voltage increase of ~110 mV over 320 h, while the BZY-15 cell has only ~10 mV increases over 500 h. The slight increase in voltage of the BZY cell may result from degradation of the oxygen electrode and the oxygen electrode/electrolyte interface. We further analysed the EIS (measured at a direct current bias of −1 A cm^{-2}) of the BZY-15 and BCZYYb cells before and after the stability tests. We found minimal increase in the ohmic resistance (the left intercept of the depressed semi-circle with the *x* axis; 0.197 Ω cm^2 before testing and 0.200 Ω cm^2 after testing) and the polarization resistance (the diameter of the depressed semi-circle; 0.026 Ω cm^2 before testing and 0.026 Ω cm^2 after testing) of the BZY-15 cell (Fig. 3c), while the BCZYYb cell (Fig. 3d) shows substantial increases in both the ohmic resistance (0.175 Ω cm^2 before testing and 0.210 Ω cm^2 after testing, increased by 20%) and the polarization resistance (0.030 Ω cm^2 before testing and 0.057 Ω cm^2 after testing, increased by 90%). This is despite the fact that the BCZYYb cell does have good stability under low steam pressures, such as 0.03 atm steam, as shown by the grey curve in Supplementary Fig. 10. As also compared in Supplementary Fig. 10, the stability of the BCZYYb cell worsens as the steam pressure increases, and even at −1 A cm^{-2} and 0.5 atm steam, the cell voltage increases continuously and by 80 mV over 500 h, and the delamination of the oxygen electrode can be easily observed in the fractured surface of the tested cell (Supplementary Fig. 11). For further verification of the material stability, we exposed sintered BZY pellets to 50% steam at 600 °C for 300 h and found no impurity peaks (see X-ray diffraction (XRD) and Raman data in Supplementary Figs. 12 and 13) after the treatment. Therefore, the superior stability of BZY-15 in high-steam pressure electrolysis has been demonstrated, and the performance and stability of high-current density PCEC can be further increased by improving the catalytic activity and sinterability of the oxygen electrode materials and by optimizations in the testing schedule, such as intermittent switches from PCEC to PCFC operations[48,49].

https://doi.org/10.1038/s44160-025-00765-z

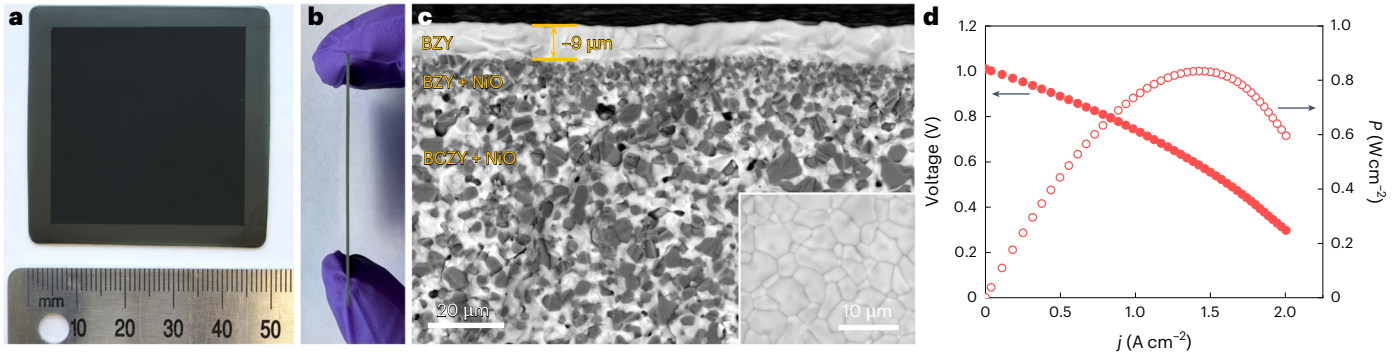

Fig. 5 | A 50 × 50 mm² square cell with thin electrolyte. a,**b**, Top (**a**) and side (**b**) view of the fabricated square cell with a 9-µm-thick electrolyte membrane. **c**, The microstructure of the fracture surface. Inset: the microstructure of the electrolyte surface. **d**, PCFC performance at different current densities, *j*, at 600 °C. The filled circle data points relate to voltage, and hollow circle data points relate to power density, *P*.

Benchmarking BZY cell performance

Having clarified the electrolysis stability and Faradaic efficiency advantages, we now push the performance limit of BZY full cells by thinning down the electrolyte membrane and modifying the oxygen electrode/electrolyte interface[50]. Instead of adopting solution-derived methods, we used scalable tape casting to fabricate ultrathin electrolyte membrane and protonic cells. With the same design and co-sintering condition, we successfully fabricated BZY cells with a ~5-µm-thick dense electrolyte. The electrochemical performance is shown in Supplementary Fig. 14a–c. The fractured surface and the electrolyte surface (Supplementary Fig. 15) of the half-cell show a dense, coarse-grained microstructure (Interestingly, the average grain size is ~7.2 µm, which is ~2 times larger than that of BZY-15 in Fig. 1a, despite the same sintering condition).

The obtained BZY cells with 5-µm-thick electrolyte treated by concentrated nitric acid for 10 min (denoted as BZY-5 hereafter) have unprecedented performance, as shown in Fig. 4 and Supplementary Fig. 14d. Under PCFC operations (Fig. 4a and Supplementary Fig. 16a), BZY-5 cell demonstrates a P_{max} of 1.24 W cm^{-2} at 600 °C, 0.91 W cm^{-2} at 550 °C, 0.75 W cm^{-2} at 500 °C, 0.57 W cm^{-2} at 450 °C and 0.31 W cm^{-2} at 400 °C. Under PCEC operations (Fig. 4b and Supplementary Fig. 16b), BZY-5 cell demonstrates high-current densities of −2.33 A cm^{-2} at 600 °C, −1.63 A cm^{-2} at 550 °C, −1.0 A cm^{-2} at 500 °C, −0.56 A cm^{-2} at 450 °C and −0.22 A cm^{-2} at 400 °C at an applied voltage of 1.3 V. These results represent major performance leaps in protonic zirconate cells (most literature reports on zirconate cells used sintering aids to facilitate sintering, which is detrimental to the electrochemical properties and cell performance). Specifically, the P_{max} of PCFC (Fig. 4c) is doubled at 600 °C and tripled at 450 °C over the best literature data (which is expected to be more pronounced at even lower temperatures considering the weak temperature dependence of our BZY-5), and the electrolysis current density (Fig. 4d) is again tripled at 450–600 °C over the best literature data (the enhanced Faradaic efficiency in our case is not counted due to limited information in the literature).

For completeness, we measured the Faradaic efficiency of BZY-5 cells under different steam pressures (balanced by air) and current densities at 600 °C (Fig. 4e). Owing to the better performance and lowered internal resistances, we were able to measure the Faradaic efficiency at 0.2–0.7 atm stream pressure and current density up to −4 A cm^{-2}. The beneficial role of high steam pressure is again demonstrated. At 0.7 atm stream pressure, the Faradaic efficiency can be maintained at 91% at −1 A cm^{-2} and a satisfactory value of 65% at current density as large as −4 A cm^{-2}. Figure 4f shows the generated H_2 outflux at different applied voltages. At 1.41 V and 0.7 atm steam pressure, it can reach as large as 19.62 ml min^{-1} cm^{-2}.

Discussion

We have demonstrated dense BZY membrane based full cells with excellent electrochemical performance and stability in acidic high-pressure steam and under harsh electrochemical conditions. The degradation under 0.7 atm steam at 600 °C, suppressed in BZY cells and pronounced in BCZYYb cells, shares some similarities with high-temperature pressurized water corrosion under autoclave conditions, which is known to dissolve many oxides. Material- and device-level stabilities are the key to emerging green-energy applications under chemically extreme conditions. In this sense, even though the present BZY conductivity realized in our electrochemical full cell is lower than what has recently been demonstrated for BCZYYb in full cells, BZY could still win many applications, such as high-current density water electrolysis where high steam pressure is preferred, as well as the deprotonation of ethane to co-generate ethylene and hydrogen where highly reducing conditions are imposed on both electrodes. Meanwhile, more optimizations in materials synthesis, device processing and oxygen electrode material/microstructure design could further improve the performance of protonic zirconate cells towards practical applications. One such effort we have undertaken is to fabricate large-area square cells (50 × 50 mm²) with 9-µm-thick dense electrolytes using the approach reported in this work. The photographs of the fabricated cells are shown in Fig. 5a,b, with no damage or shape distortions. The mechanical strengths of the half-cell with the cell configuration of BCZY + NiO/BZY + NiO/BZY are evaluated and compared with the BCZYYb + NiO/BCZYYb half-cell, as shown in Supplementary Fig. 17. The microstructure of the sintered electrolyte with 9 µm thickness is dense and has a coarse grain size (Fig. 5c). Figure 5d shows the PCFC performance of the square cell at 600 °C, with a P_{max} of 0.84 W cm^{-2}. Considering the high performance obtained for these BZY square cells and the progressive improvements and lessons learned in protonic ceramic cells in the past 10 years, we are optimistic about future developments of BZY PCFCs/PCECs. Evaluations of long-term PCFC and PCEC stability and Faradaic efficiency of such large-area cells under practical operational conditions would benefit the future development of the field.

Conclusions

By redesigning the architecture of the BZY full cell, we have offered a solution to the dense BZY membrane sintering conundrum and unlocked the excellent electrochemical performance and stability of BZY-based PCFCs/PCECs, especially under high-current density, high-steam pressure electrolysis. The revisited protonic zirconate cells are promising in hydrogen and chemical productions with moderate thermal budgets and demanding yet rewarding electrochemical conditions. Our work highlights the critical role of processing innovations, such as (co-)sintering, to fully deliver materials' intrinsic advantages for targeted applications.

Methods

Materials synthesis

BCZY and BZY were synthesized by a solid-state method. Stoichiometric amounts of $BaCO_3$ (99.8% purity, Alfa Aesar), ZrO_2 (99.9% purity, Alfa Aesar), CeO_2 (99.9% purity, Alfa Aesar) and Y_2O_3 (99.9% purity, Alfa Aesar) were mixed by ball milling in ethanol for 24 h, followed by drying, grinding and heat treatment at 1,300 °C for 10 h to obtain phase-pure crystallized BZY and BZCY powders, as verified by XRD in Supplementary Fig. 18. Oxygen electrode material $PrNi_{0.7}Co_{0.3}O_{3-\delta}$ was synthesized by a wet-chemistry method. Stoichiometric amounts of $Pr(NO_3)_3{\cdot}6H_2O$(99.99% purity, Alfa Aesar), $Ni(NO_3)_2{\cdot}6H_2O$ (99.9985% purity, Alfa Aesar) and $Co(NO_3)_2{\cdot}6H_2O$ (99.999% purity, Alfa Aesar) were dissolved in deionized water to form a homogeneous solution with 0.05 mol l^{-1} cation concentration (Pr + Ni + Co in total). Glycol and citric acid were next added into the solution in a mole ratio of glycine:citric acid: (Pr + Ni + Co) of 2:1:1. The as-prepared solution was heated on a hot plate with continuous stirring until a gel was formed. The obtained gel was heat treated at 400 °C, followed by an auto-ignition process to produce a black foamy intermediate product. The final $PrNi_{0.7}Co_{0.3}O_{3-\delta}$ powders were obtained by heat treating the intermediate product at 1,000 °C for 4 h (see the XRD in Supplementary Fig. 19 and microstructure in Supplementary Fig. 20).

Cell fabrications

Hydrogen electrode-supported cells were fabricated by a tape casting process. To prepare green tapes of the BCZY + NiO supporting layer, NiO and BCZY powders were mixed with 6:4 weight ratio by ball milling in ethanol and toluene for 24 h. Binder of polyvinyl butyral, plasticizer of butyl benzyl phthalate and dispersant of fish oil were next added, followed by ball milling for an additional 24 h to obtain the desired rheology. Tape casting was performed on a laboratory tape casting machine with a controlled thickness of ~300 μm after sintering. Green tapes of BCZY + NiO supporting layer, BZY + NiO buffer layer and BZY electrolyte layer were similarly prepared with controlling their thicknesses (after sintering) to be ~300 μm, ~25 μm and ~14 μm, respectively.

To prepare BCZY + NiO|BZY + NiO|BZY trilayer as the half-cell, three pieces of BCZY + NiO supporting-layer green tapes, one piece of BZY + NiO buffer layer green tape and one piece of BZY electrolyte green tape were laminated by a hot press at 70 °C under an applied pressure of 4 ton for 5 h. We fabricated half-cells with three different sizes and shapes: a disc shape with 10 mm diameter and 15 μm electrolyte thickness, a disc shape with 1 inch diameter and 5 μm electrolyte thickness and a square shape with 50 × 50 mm^2 area and 9 μm electrolyte thickness. The laminated green tapes were punched with 11 mm (7/16 inch) diameter holes and pre-sintered at 920 °C for 3 h to remove the organics. Co-sintering of BCZY + NiO|BZY + NiO|BZY for later-on full cell fabrications and testing was conducted at T_1 = 1,450 °C for 10 h in air (heating schedule: 3 °C min^{-1} heating rate to 1,000 °C, holding at 1,000 °C for 1 h and 2 °C min^{-1} heating rate to 1,450 °C), followed by 3 °C min^{-1} cooling down to room temperature. The BZY + NiO|BZY bilayer was prepared similarly by using BZY + NiO supporting-layer green tapes and sintering conditions described in the main text. The PCECs with electrolyte thickness of 5 μm were fabricated following the above procedures with thinner electrolyte layer and laminated green tapes of BCZY + NiO|BZY + NiO|BZY were punched with the diameter of 28.58 mm (1.125 inch). The planar PCECs with larger size of 50 × 50 mm^2 were also fabricated according to above-mentioned specifications with laminated green tape size of 62.5 × 62.5 mm^2. The difference comes from the sintering process, in which the pre-sintered body needed to be protected by sintered BZY20 powders under the same sintering temperature programme.

To fabricate full cells, a slurry of the oxygen electrode material $PrNi_{0.7}Co_{0.3}O_{3-\delta}$ was prepared by mixing $PrNi_{0.7}Co_{0.3}O_{3-\delta}$ powders with ethanol and a texanol-based binder by ball milling and then brush-painted on the electrolyte surface of the co-sintered half-cell. The painted cells were heat treated at T_2 = 1,000 °C for 5 h (heating schedule: 2 °C min^{-1} heating rate to 600 °C, holding at 600 °C for 1 h and 3 °C min^{-1} heating rate to 1,000 °C), followed by 3 °C min^{-1} cooling down to room temperature.

Characterizations

XRD measurements were conducted on a D8ADVANCE/Bruker X-ray diffractometer using Ni-filter Cu Kα radiation (wavelength of 0.154056 nm). The microstructure was inspected under SEM (JEOL 6700F). To prepare the sample for TEM analysis, the cell was cut into small pieces (1 × 2.2 mm^2) then face-to-face bonded together by conductive epoxy, followed by mechanical thinning, dimpling and Ar^+ milling at 4.2 kV using Gatan PIPS. An FEI Tecnai F30 super-twin field-emission-gun TEM operated at 300 kV was used to collect TEM images and annular dark-field scanning transmission electron microscopy images. A Gatan Tridiem 863 UHS GIF system was used to acquire the EELS spectra. The Raman spectra were obtained using a customized Renishaw inVia Spectro microscopy system with an Olympus 20× objective. A He–Ne laser (633 nm) was used for spectral excitation. The porosity of the half-cell with the configuration of BCZY + NiO|BZY-15 + NiO|BZY was measured by porosimeter. Pore size was measured by mercury injection capillary pressure (AutoPore IV, Micromeritics). Proton conductivity σ is calculated by $\sigma = 1/\rho = L/RA$, where ρ is the electrolyte resistivity (in Ω cm), L is the electrolyte thickness (in cm), A is the effective area of the electrolyte (in cm^2) and R is the resistance (in Ω). The flatness of the BZY-15 cells was characterized by a Wide-Area 3D Measurement System (KEYENCE, VR Series). The flexural strength of the sintered half-cells was measured using a dynamic mechanical analyser (TA Instruments, Waters LLC, DMA 850) as shown in Supplementary Figs. 17a and 7b. The properties were determined with a three-point bending clamp. The equipment was calibrated after preheating for 30 min. The initial force was set as 0.01 N. The flexural strength test was carried at room temperature with the ramp rate of 0.5 mm min^{-1}. At least eight specimens of two materials were tested. Flexural strength was calculated using the following equation: flexural strength = $3Fl/2bd2$, where F is the ultimate failure load (in N), l is the effective span (length of both ends of the clamp (in 10 mm)) and b and d are the width and thickness of the sample (in mm), respectively.

Electrochemical measurements

Hydrogen electrode-supported full cells were sealed by a glass sealant (Mo-sci GL1745) onto a home-made testing fixture. Gold mesh was used as the current collector with attached gold wires as the leads. After the curing procedure of the glass sealant, the cell was heated up to the testing temperature (heating rate of 1 °C min^{-1}). The 50 × 50 mm^2 square PCECs were sealed in a set of stainless-steel manifolds with additional Mica gaskets to enhance the sealant performance. Specifically, glass sealant was applied at each interface between the cell and the gasket, as well as between the gasket and the manifold piece. When the set temperature was reached, H_2 (with a flow rate of 20 ml min^{-1} for the 10 mm cell, 40 ml min^{-1} for the 1 inch cell or 100 ml min^{-1} for the square cell) was fed into the hydrogen electrode to reduce NiO to metallic Ni. When the reduction process was completed, a temperature-controlled humidifier was connected between the gas inlet of the hydrogen electrode and the inward gas to hydrolyse H_2 with steam.

Electrochemical data under fuel cell and electrolysis modes were collected on an electrochemical workstation (Solartron 1400). Under the fuel cell mode, the feedstock for the oxygen electrode was pure oxygen with flow rate of 40 ml min^{-1} for the 10 mm cell, 100 ml min^{-1} for the 1 inch cell and 200 ml min^{-1} for the square cell, and the feedstock for the hydrogen electrode was H_2 with 3% steam. After a stable OCV was observed at the set temperature, EIS measurements were conducted under OCV conditions at 450–600 °C with a frequency range from 10^5 to 0.1 Hz and an a.c. amplitude of 20 mV, and current density–voltage

curves and current density–power density curves were measured. Then, the testing condition was switched to the electrolysis mode, where the feedstock was H_2 (with a flow rate of 20 ml min^{-1} for the 10 mm cell, 40 ml min^{-1} for the 1 inch cell and 100 ml min^{-1} for the square cell) for the hydrogen electrode and humidified air (20% steam) for the oxygen electrode with air flow rate of 100 ml min^{-1} for the 10 mm cell, 200 ml min^{-1} for the 1 inch cell and 400 ml min^{-1} for square cell. Electrochemical tests were conducted after a stable OCV was observed at the set temperature, at a voltage range from OCV to 1.5 V. The Faradaic efficiency was tested by a mass flow meter-based measurement. First, the off-gas flow rate under OCV condition was tested by the mass flow rate to establish the baseline. Then, the PCEC was operated under the electrolysis mode at a constant current density. After the voltage was stable for 20 min, the off-gas flow rate was tested by the mass flow meter. The average results were obtained after testing five times with a fluctuation of less than 5%. Finally, the Faradaic efficiency was calculated from the produced hydrogen amount.

Hydrogen production rates under different steam concentrations (0.2 atm, 0.5 atm and 0.7 atm steam, balanced with air) were measured by applying a constant current on the BZY cell and monitoring the hydrogen outflow rate. At each testing condition, the hydrogen production rate was calculated by subtracting the H_2 outflow rate under OCV condition from the H_2 outflow rate under electrolysis operation. The calculated hydrogen production rate was converted to protonic current density to calculate the Faradaic efficiency.

Long-term stability test of BZY full cells was conducted under 0.5 atm and 0.7 atm steam condition (balanced with air) over 800 h at 600 °C, with the following schedule: at −1 A cm^{-2} current density and 0.5 atm steam from the beginning to hour 200, at −0.5 A cm^{-2} and 0.5 atm steam from hour 200 to hour 400, at −1.5 A cm^{-2} and 0.5 atm steam from hour 400 to hour 600, at −1 A cm^{-2} and 0.7 atm steam from hour 600 to hour 700 and at −2 A cm^{-2} and 0.7 atm steam from the hour 700 to hour 800. Faradic efficiency was measured intermittently throughout the test. Long-term stability tests comparing BZY and BCZYYb full cells were conducted under 0.7 atm steam condition (balanced with air) at −1 A cm^{-2} current density at 600 °C over 500 h for BZY full cell and 320 h for BCZYYb full cell. EIS measurements were conducted before and after the long-term stability tests, with a frequency range from 10^5 to 0.1 Hz, a direct current (d.c.) bias of −1 A cm^{-2} and an a.c. amplitude of 10 mA (corresponding to 56 mA cm^{-2}).

Data availability

Data supporting the findings in the present work are available in the manuscript or Supplementary Information.

References

1. Fabbri, E. et al. Tailoring the chemical stability of $Ba(Ce_{0.8-x}Zr_x)Y_{0.2}O_{3-\delta}$ protonic conductors for intermediate temperature solid oxide fuel cells (IT-SOFCs). *Solid State Ion.* **179**, 558–564 (2008).
2. Ding, H. et al. Self-sustainable protonic ceramic electrochemical cells using a triple conducting electrode for hydrogen and power production. *Nat. Commun.* **11**, 1907 (2020).
3. Kim, J. et al. Triple-conducting layered perovskites as cathode materials for proton-conducting solid oxide fuel cells. *ChemSusChem* **7**, 2811–2815 (2014).
4. Wachsman, E. D. & Lee, K. T. Lowering the temperature of solid oxide fuel cells. *Science* **334**, 935–939 (2011).
5. Wu, W. et al. Electrochemically engineered, highly energy-efficient conversion of ethane to ethylene and hydrogen below 550 °C in a protonic ceramic electrochemical cell. *ACS Catal.* **11**, 12194–12202 (2021).
6. Vøllestad, E. et al. Mixed proton and electron conducting double perovskite anodes for stable and efficient tubular proton ceramic electrolysers. *Nat. Mater.* **18**, 752–759 (2019).
7. Li, M. et al. Switching of metal–oxygen hybridization for selective CO_2 electrohydrogenation under mild temperature and pressure. *Nat. Catal.* **4**, 274–283 (2021).
8. Virkar, A. V. Mechanism of oxygen electrode delamination in solid oxide electrolyzer cells. *Int. J. Hydrog. Energy* **35**, 9527–9543 (2010).
9. Jacobsen, T. & Mogensen, M. The course of oxygen partial pressure and electric potentials across an oxide electrolyte cell. *ECS Trans.* **13**, 259 (2008).
10. Dong, Y. et al. Potential jumps at transport bottlenecks cause instability of nominally ionic solid electrolytes in electrochemical cells. *Acta Mater.* **199**, 264–277 (2020).
11. Yang, L. et al. Enhanced sulfur and coking tolerance of a mixed ion conductor for SOFCs: $BaZr_{0.1}Ce_{0.7}Y_{0.2-x}Yb_xO_{3-\delta}$. *Science* **326**, 126–129 (2009).
12. Katahira, K. et al. Protonic conduction in Zr-substituted $BaCeO_3$. *Solid State Ion.* **138**, 91–98 (2000).
13. Chen, F. et al. Chemical stability study of $BaCe_{0.9}Nd_{0.1}O_{3-\alpha}$ high-temperature proton-conducting ceramic. *J. Mater. Chem.* **7**, 481–485 (1997).
14. Bhide, S. V. & Virkar, A. V. Stability of $BaCeO_3$-based proton conductors in water-containing atmospheres. *J. Electrochem. Soc.* **146**, 2038 (1999).
15. Li, J. et al. Chemical stability of Y-doped Ba(Ce, Zr)O_3 perovskites in H_2S-containing H_2. *Electrochim. Acta* **53**, 3701–3707 (2008).
16. Shin, S. et al. Protonic conduction in the single crystals of $SrZrO_3$ and $SrCeO_3$ doped with Y_2O_3. *Solid State Ion.* **40**, 910–913 (1990).
17. Mitsui, A., Miyayama, M. & Yanagida, H. Evaluation of the activation energy for proton conduction in perovskite-type oxides. *Solid State Ion.* **22**, 213–217 (1987).
18. Takahashi, T. & Iwahara, H. Solid-state ionics: protonic conduction in perovskite type oxide solid solutions. *Rev. Chim. Min.* **17**, 243–253 (1980).
19. Kreuer, K. D. Proton-conducting oxides. *Annu. Rev. Mater. Res.* **33**, 333–359 (2003).
20. Ryu, K. H. & Haile, S. M. Chemical stability and proton conductivity of doped $BaCeO_3$–$BaZrO_3$ solid solutions. *Solid State Ion.* **125**, 355–367 (1999).
21. Fabbri, E., Pergolesi, D. & Traversa, E. Materials challenges toward proton-conducting oxide fuel cells: a critical review. *Chem. Soc. Rev.* **39**, 4355–4369 (2010).
22. Babilo, P., Uda, T. & Haile, S. M. Processing of yttrium-doped barium zirconate for high proton conductivity. *J. Mater. Res.* **22**, 1322–1330 (2007).
23. Choi, S., Davenport, T. C. & Haile, S. M. Protonic ceramic electrochemical cells for hydrogen production and electricity generation: exceptional reversibility, stability, and demonstrated faradaic efficiency. *Energy Environ. Sci.* **12**, 206–215 (2019).
24. Melekh, B.-T. et al. Structure, phase transitions and optical properties of pure and rare earth doped $BaCeO_3$, $SrCeO_3$ prepared by inductive melting. *Solid State Ion.* **97**, 465–470 (1997).
25. Yamanaka, S. et al. Thermophysical properties of $BaZrO_3$ and $BaCeO_3$. *J. Alloys Compd.* **359**, 109–113 (2003).
26. Arabacı, A. & Öksüzömer, M. F. Preparation and characterization of 10 mol% Gd doped CeO_2 (GDC) electrolyte for SOFC applications. *Ceram. Int.* **38**, 6509–6515 (2012).
27. Zhang, S. L. et al. Effect of Fe doping on the performance of suspension plasma-sprayed $PrBa_{0.5}Sr_{0.5}Co_{2-x}Fe_xO_{5+\delta}$ cathodes for intermediate-temperature solid oxide fuel cells. *Ceram. Int.* **43**, 11648–11655 (2017).
28. Zha, S. et al. GDC-based low-temperature SOFCs powered by hydrocarbon fuels. *J. Electrochem. Soc.* **151**, A1128 (2004).
29. Peng, C. et al. $BaZr_{0.8}Y_{0.2}O_{3-\delta}$ electrolyte with and without ZnO sintering aid: preparation and characterization. *Solid State Ion.* **181**, 1372–1377 (2010).

30. Shimada, H. et al. Effect of Ni diffusion into $BaZr_{0.1}Ce_{0.7}Y_{0.1}Yb_{0.1}O_{3-\delta}$ electrolyte during high temperature co-sintering in anode-supported solid oxide fuel cells. *Ceram. Int.* **44**, 3134–3140 (2018).
31. Okuyama, Y. et al. Improvement of protonic ceramic fuel cells with thin film BCZY electrolyte. *ECS Trans.* **68**, 2545 (2015).
32. Dong, Y. et al. Enhanced mobility of cations and anions in the redox state: the polaronium mechanism. *Acta Mater.* **232**, 117941 (2022).
33. Han, D. et al. Proton conductive $BaZr_{0.8-x}Ce_xY_{0.2}O_{3-\delta}$: influence of NiO sintering additive on crystal structure, hydration behavior, and conduction properties. *ChemSusChem* **14**, 614–623 (2021).
34. Huang, Y., Merkle, R. & Maier, J. Effect of NiO addition on proton uptake of $BaZr_{1-x}Y_xO_{3-x/2}$ and $BaZr_{1-x}Sc_xO_{3-x/2}$ electrolytes. *Solid State Ion.* **347**, 115256 (2020).
35. Han, D. et al. Detrimental effect of sintering additives on conducting ceramics: yttrium-doped barium zirconate. *ChemSusChem* **11**, 4102–4113 (2018).
36. Liu, Z. et al. Enhancing sinterability and electrochemical properties of $Ba(Zr_{0.1}Ce_{0.7}Y_{0.2})O_{3-\delta}$ proton conducting electrolyte for solid oxide fuel cells by addition of NiO. *Int. J. Hydrog. Energy* **43**, 13501–13511 (2018).
37. Vera, C. Y. R. et al. A mini-review on proton conduction of $BaZrO_3$-based perovskite electrolytes. *J. Phys. Energy* **3**, 032019 (2021).
38. Dong, Y. et al. Ultra-uniform nanocrystalline materials via two-step sintering. *Adv. Funct. Mater.* **31**, 2007750 (2021).
39. Kjølseth, C. et al. Space–charge theory applied to the grain boundary impedance of proton conducting $BaZr_{0.9}Y_{0.1}O_{3-\delta}$. *Solid State Ion.* **181**, 268–275 (2010).
40. Sun, Z. et al. Electrochemical properties and intermediate-temperature fuel cell performance of dense yttrium-doped barium zirconate with calcium addition. *J. Am. Ceram. Soc.* **95**, 627–635 (2012).
41. Sun, W., Liu, M. & Liu, W. Chemically stable yttrium and tin co-doped barium zirconate electrolyte for next generation high performance proton-conducting solid oxide fuel cells. *Adv. Energy Mater.* **3**, 1041–1050 (2013).
42. Sun, W. et al. An easily sintered, chemically stable, barium zirconate-based proton conductor for high-performance proton-conducting solid oxide fuel cells. *Adv. Funct. Mater.* **24**, 5695–5702 (2014).
43. Shafi, S. P. et al. Y and Ni co-doped $BaZrO_3$ as a proton-conducting solid oxide fuel cell electrolyte exhibiting superior power performance. *J. Electrochem. Soc.* **162**, F1498–F1503 (2015).
44. Shi, N. et al. Controllable CO_2 conversion in high performance proton conducting solid oxide electrolysis cells and the possible mechanisms. *J. Mater. Chem. A* **7**, 4855–4864 (2019).
45. Lei, L. et al. Energy storage and hydrogen production by proton conducting solid oxide electrolysis cells with a novel heterogeneous design. *Energy Convers. Manag.* **218**, 113044 (2020).
46. Dong, Y. et al. Chemical and structural origin of hole states in yttria-stabilized zirconia. *Acta Mater.* **203**, 116487 (2021).
47. Kim, I.-H. et al. Determination of partial conductivities and computational analysis of the theoretical power density of $BaZr_{0.1}Ce_{0.7}Y_{0.1}Yb_{0.1}O_{3-\delta}$ (BZCYYb1711) electrolyte under various PCFC conditions. *J. Mater. Chem. A* **7**, 21321–21328 (2019).
48. Graves, C. et al. Eliminating degradation in solid oxide electrochemical cells by reversible operation. *Nat. Mater.* **14**, 239–244 (2015).
49. Skafte, T. L. et al. Electrothermally balanced operation of solid oxide electrolysis cells. *J. Power Sources* **523**, 231040 (2022).
50. Bian, W. et al. Revitalizing interface in protonic ceramic cells by acid etch. *Nature* **604**, 479–485 (2022).
51. Sun, Z. et al. Lowering grain boundary resistance of $BaZr_{0.8}Y_{0.2}O_{3-\delta}$ with $LiNO_3$ sintering-aid improves proton conductivity for fuel cell operation. *Phys. Chem. Chem. Phy.* **13**, 7692–7700 (2011).
52. Luisetto, I. et al. Electrochemical performance of spin coated dense $BaZr_{0.8}0Y_{0.16}Zn_{0.04}O_{3-\delta}$ membranes. *J. Power Sources* **220**, 280–285 (2012).
53. Lei, L. et al. A highly active hybrid catalyst modified $(La_{0.60}Sr_{0.40})_{0.95}Co_{0.20}Fe_{0.80}O_{3-\delta}$ cathode for proton conducting solid oxide fuel cells. *J. Power Sources* **389**, 1–7 (2018).
54. Duan, C. et al. Readily processed protonic ceramic fuel cells with high performance at low temperatures. *Science* **349**, 1321–1326 (2015).
55. Bi, L. et al. Y-doped $BaZrO_3$ as a chemically stable electrolyte for proton-conducting solid oxide electrolysis cells (SOECs). *J. Mater. Chem. A* **3**, 5815–5819 (2015).
56. Lei, L. et al. Intermediate-temperature solid oxide electrolysis cells with thin proton-conducting electrolyte and a robust air electrode. *J. Mater. Chem. A* **5**, 22945–22951 (2017).

Acknowledgements

This work is supported by the proton conducting solid oxide electrolysis cells (P-SOEC) lab call project and the HydroGEN Advanced Water Splitting Materials Consortium, established as part of the Energy Materials Network under the United States Department of Energy (USDOE); the Office of Energy Efficiency and Renewable Energy (EERE); and the Hydrogen and Fuel Cell Technologies Office (HFTO) under DOE Idaho Operations Office under contract no. DE-AC07-05ID14517. We would like to thank the Office of EERE and the Office of Basic Energy Sciences (BES) for support through H2LinkSc, a cross-office initiative to bring new ideas, materials, and tools from basic science to bear on applied problems. H.L. and M.Z. also would like to acknowledge funding support from National Science Foundation (OIA-2119688) and a subcontract from Idaho National Laboratory. J.L. acknowledges support by the Hydrogen in Energy and Information Sciences (HEISs), an Energy Frontier Research Center funded by the U.S. Department of Energy (DOE), Office of Science, Basic Energy Sciences (BES), under Award DE-SC0023450.

Author contributions

Y. Dong, H.L., J.L. and D.D. conceived the project. W.T., W.B. and H.D. fabricated the cells and conducted electrochemical measurements. W.T., W.B. and Y. Dong analysed the data. Y. Ding conducted the TEM analysis. Z.Z., Q.S. and S.K. contributed to the SEM analysis and cell fabrication. Q.S., Y.W., B.X., P.D., D.C., J.Y.G., W.F., W.W. and M.Z. contributed to sample characterizations and analysis. W.T., W.B. and Y. Dong wrote the paper, with substantial inputs from H.D., H.L., J.L. and D.D. All authors discussed and contributed to the writing.

Competing interests

The authors declare no competing interests.

Additional information

Supplementary information The online version contains supplementary material available at https://doi.org/10.1038/s44160-025-00765-z.

Correspondence and requests for materials should be addressed to Yanhao Dong, Hongmei Luo, Ju Li or Dong Ding.

Peer review information *Nature Synthesis* thanks Guntae Kim and the other, anonymous, reviewer(s) for their contribution to the peer review of this work. Primary Handling Editor: Peter Seavill, in collaboration with the *Nature Synthesis* team.